CARNEGIE MELLON UNIVERSITY

Manufacturing of a 3D Soft Sensor for Feedback Control of Pneumatic Muscles and Applications with Cylindrical Structures

by

Luis Valle

A thesis submitted in partial fulfillment for the
degree of Master of Science in Robotics

in the

Computer Science Department
The Robotics Institute

December 2017

Declaration of Authorship

I, Luis Valle, declare that this thesis titled, 'Manufacturing of a 3D Soft Sensor for Feedback Control of Pneumatic Muscles and Applications with Cylindrical Structures' and the work presented in it are my own. I confirm that:

- This work was done wholly or mainly while in candidature for a research degree at this University.
- Where any part of this thesis has previously been submitted for a degree or any other qualification at this University or any other institution, this has been clearly stated.
- Where I have consulted the published work of others, this is always clearly attributed.
- Where I have quoted from the work of others, the source is always given. With the exception of such quotations, this thesis is entirely my own work.
- I have acknowledged all main sources of help.
- Where the thesis is based on work done by myself jointly with others, I have made clear exactly what was done by others and what I have contributed myself.

Signed: 

Date: 12/29/2017

"Why would a quantum field care about doing what it does? Why does it just 'not do' instead of 'doing'?"

CARNEGIE MELLON UNIVERSITY

Abstract

Computer Science Department
The Robotics Institute

Master of Science in Robotics

by Luis Valle

Presented is the manufacturing process and characterization of a 3-D Helical soft sensor composed of Eutectic Gallium Indium (eGaIn) as the conductive pattern and silicone rubber as the substrate. A novel eGaIn writing process was used to achieve the 3D structure. The process did not require any molds. Different diameter sensors and coil densities are shown to show repeatability and versatility of the process. A multilayer sensor is also shown. Some example applications for the sensors are shown. Sensors were tested up to deformations of 50% diametrically and 21% axially. Diametrically, resistance changes of up to 20 Ω are achieved. The results show negligible hysteresis diametrically and a change of 0.2 Ω axially, showing the sensor to be sensitive, reliable, and compact solution for applications where diameter change needs to be measured. In addition, presented is the modeling and control of a pneumatic artificial muscle actuator with an integrated 3-D sensor for position feedback. A theoretical model and experimental characterization of the muscle-sensor package are presented with high correlation and repeatability. A position feedback sliding mode controller is implemented with a position error of <0.9% of maximum muscle contraction. Finally, further applications of the sensor are discussed.

Acknowledgements

I would like to thank God who has provided the grace to complete this thesis through circumstances, people, and virtue. I want to emphasize his patience and unconditional love towards me. I also thank my family whom without I could have not been where I am, my advisor Yong-Lae, who has provided unconditional support and patience in every step. Additionally, I would like to thank Jonathan King for his contributions in the modeling sections; Yiwei Tao for helping me with the design of the lathe, selecting components, and programing the second iteration of the syringe pump; Andrew Tallaksen for helping me setup the syringe pump in the first iteration and help with experiments, and Jin Zhu her technical support in the experiments.

Contents

List of Figures

List of Tables

Abbreviations

PAM	**P**neumatic **A**rtificial **M**uscle
eGaIn	**e**utectic **Ga**llium **In**dium
DOF	**D**egree **O**f **F**reedom
3-D	**3 D**imensional
2-D	**2 D**imensional

Physical Constants

Resistivity of eGaIn $\rho = 29.4 \times 10^{-6}$ W-cm

Symbols

For Characterization

A	Area	m^2
F	Force	N
l	Length	m
n	Number of Coils	Unitless
p	Gage Pressure	Ω
R	Resistance	Ω
r	Radius	m
s	Arc Length of Helix	m
V	Volume	m^3
α	Aspect Ratio	Unitless
ϵ	Strain	Unitless
κ	Curvature	Unitless
θ	Angle	Degrees

For Control

e	Error	m
C	Damping Coefficient	N/m
K	Spring Coefficient	N$\cdot s/m$
K_s	Sliding Mode Gain	
M	Mass	kg
u	Control Signal	
V	Lyapunov Function Candidate	
x	Position	m

σ	Sliding Manifold

Ad Maiorem Dei Gloriam...

Chapter 1

BACKGROUND

1.1 Pneumatic Artificial Muscles as Alternative Mean of Actuation

Pneumatic artificial muscles (PAMs) are a promising alternative to other types of actuators in several robotic systems [1–3]. PAMs provide advantages in applications where the local area of actuation requires high energy density, no reflected inertia, low added inertia [4], and inherent compliance [4, 5]. Yet, the advantages of PAMs could be bottlenecked by lack of compact feedback mechanisms for force and length that are conformable to the muscles. Previously, there have been rigid methods for obtaining position feedback from PAMs. Encoders [3, 6], potentiometers [7], and halleffect sensors [8] are among the most commonly used. Force feedback has also been done by using strain gauge setups [3], and gauge pressure sensing [6]. However, these rigid methods add volume and sometimes undesired additional structures, which can limit degrees of freedom (DOFs) of the system that could be useful in certain applications such as physical therapy and rehabilitation [5].

1.2 Advantages of Soft Sensors

1.2.1 When Soft Sensors are Preferable

Soft sensors have opened up new avenues for feedback in rigid and soft robotics. Although rigid sensors can achieve desired precision and accuracy, they often add undesired structures that could be simplified or eliminated with soft sensors. Encoders [3, 6], potentiometers [7], halleffect sensors [8], strain gauge setups [3], and gauge pressure sensing [6]

have been commonly used for semi-soft and rigid robotics. The rigidity of these sensors is often times not a necessary condition and a soft sensor with similar capabilities can achieve the results. In some cases, such as in physical therapy and rehabilitation [5], it is preferable for some degrees of freedom (DOFs) of the system to be unrestricted. With rigid sensors in many cases it is necessary to restrict DOFs with additional structures.

1.2.2 Advantages and Limitations of 2-D Soft Sensors

Liquid metal alloys, such as eutectic Gallium Indium or Galinstan have been popular conductive media that can be easily embedded in a soft structure, providing pressure and strain sensing capabilities. 2-D sensors have been manufactured and have shown to be useful in many applications where large deformations are necessary [5], [9], [10]. Still, it needs to be considered that the shape of these sensors depends on the use case. For instance, when measuring deflection of a planar surface, a planar sensor conforms to that particular shape very naturally. The pattern of the media is designed so sensitivity is maximized given the linear deformation of the surface. Nevertheless, when attaching this same sensor to a cylindrical surface of small radius of curvature, a pre-stress is induced, which can lead to early collapse of the channels and loss of signal. In addition, if the sensor needs to be wrapped around completely, the use of adhesives becomes necessary, which creates stress concentrators and reduce the life of the sensor.

1.2.3 Exploiting Form Factor with 3-D Soft Sensors

3-D sensors can be designed so they exploit the contour of the object with less of the limitations aforementioned. For instance, if we want to measure the radial expansion of a cylinder, pattern density can be maximized by using a 3-D coil as opposed to wrapping a 2-D sensor with a serpentine pattern. When measuring multiple degrees of freedom in a single package, 2-D sensors can be limited unless rigid components are added to them [11].

1.3 Manufacturing Challenges of 3D Soft Sensors

In addition to the current plane-bounded limitation of soft-sensors, manufacturing processes of these remain a major bottleneck. [12], [13], [14]. Only planar sensors have been mass-manufactured [15], [16]. Current methods of 3-D manufacturing require significant human skill in the loop and are not yet scalable, and require different sets of molds per configuration. In a previous work, a 3-D helical soft sensor was manufactured

through using multiple-layer casting and a low-friction thread for embedding a helical microchannel in an elastic bladder [17]. The low-friction thread would then be removed and a liquid conductor (e.g. eutectic gallium-indium, EGaIn [18]) would be injected in the channel. Some limiting factors of this process are: the diameter of the low-friction fiber being limited to small size ranges, the angle limit for the fiber to be pulled out without damaging the sensor, and how thick the polymer layer should be to prevent bubbles. This shows that 3-D manufacturing is still time-consuming and requires a dexterous manual process involved with use of complicated molds. The use of molds is particularly difficult with cylindrical surfaces. The polymer is hard to de-gas, and it is difficult to achieve a smooth surface in which a pattern can be written. The parting line of the mold is also an issue, as it reduces the smoothness necessary for eGaIn writing and introduces stress concentrations. The sensor proposed in this thesis was designed to overcome some of these challenges.

Chapter 2

RESEARCH QUESTION

2.1 The Three Pivotal Questions

This thesis is concerned with addressing the following questions:

- Is a versatile and automated method for manufacturing 3-D soft sensors possible to be developed?
- Can a 3-D soft sensor be used with advantage over other forms of sensing for feedback control of PAMs?
- Is a 3-D soft sensor versatile? Can it be used for applications other than PAMs?

2.2 How the Questions were Addressed

2.2.1 Response to Question 1

I present a new manufacturing method of a 3-D helical pattern sensor which consists of a three-step process using a modified lathe. For the first step, a new method of manufacturing a thin cylindrical polymer structure without using a mold was developed. For the subsequent steps in the process, coil density, length, and diameter of the sensor can be controlled. The process does not require molds or low-friction thread. This is explained with more detail in section 4.1.

2.2.2 Response to Question 2

The 3-D soft sensor built exploits form factor from the actuation source with minimal extra volume. This provides weight and volume advantages over traditional rigid means of sensing. In addition, presented is the characterization of the sensor in the axial, diametrical, and torsional modes, found in section 4.2. In addition, a theoretical model of the resistance to muscle length mapping is presented, which highly matches the experimental data[1]. Sensors with coil densities of 14 coils/cm with a resistance range of of 11.4 to 22.4 Ω for a range of 25% contraction have been achieved. After the Characterization, a stability analysis and implementation of position feedback control of the PAM-sensor package were achieved using sliding mode.

2.2.3 Response to Question 3

The sensor can be quickly integrated to any existing pneumatic muscle of cylindrical geometry. Further experiments for future applications are shown in section 5.3.1.

[1] Model provided by Jonathan King

Chapter 3

RELATED WORK

Two-dimensional soft sensors have been designed for sensing displacement and pressure and have the potential to accommodate for these needs [5], [14]. Position feedback control has been demonstrated with these sensors with the advantage of relaxed form factors but with comparable results to rigid methods [5]. These sensors allow for less adverse effects to natural DOFs of the system. These work well for position sensing, conforming to some geometry of the system to be controlled, but they do not conform to the geometry of the source of actuation directly, which tend to be PAMs. Three-dimensional (3-D) helical soft sensors have been manufactured as a package with Kevlar-fiber embedded PAMs [17]. Still, coil density and hence sensitivity, are limited by this manufacturing process, and the sensor remains coupled to this particular PAM.

No feedback control has yet been implemented for this type of package. Other monolithic sensors/actuators have been designed [19], but with difficult transferability to commonly used actuation methods.

Another type of self-contained sensing PAMs is to either braid or wrap a conductive wire (e.g. copper wire) on a McKibben-type PAM following the mesh pattern for measuring inductance change of the wire with contraction of the muscle [20, 21]. The integration of the sensing element with the muscle involves with manual processes and may cause manufacturing errors in this case.

Chapter 4

METHODS

4.1 Manufacturing Process

The sensor is a hollow cylinder made of silicone rubber with an internal eGaIn[1] helical pattern. Examples of the sensor can be seen in figure 5.7. The process of fabrication of the sensor consists of three stages: 1) An Initial cylindrical polymer layer. 2) eGaIn writing on the layer. 3) Covering the eGaIn spiral with another polymer layer. A modified mini-lathe[2] with two automated DOFs was used to manufacture the sensor.

4.1.1 Concept/Modeling

4.1.1.1 Polymer Layer

The goal for the first stage of the process is to obtain a thin cylindrical silicone structure. Since silicone has shearing strain characteristics prior to curing, an intuitive way to obtain a final form with desired shape is to constrain the material within a solid until it cures. This is the principle on which molds operate. An alternative method is to exploit the characteristics of the material in order to minimize the constraints required in the manufacturing system. To do this, knowing the behavior of the materials to be used is beneficial. In figure 4.1 it can be seen that the three types of silicone used for the experiment can be considered Newtonian under the relatively low speed characteristic of our system.

If a drop of Newtonian fluid is dropped on a rotating cylinder, provided that it is viscous enough and the cylinder is rotating with enough speed, the fluid will remain

[1] Eutectic Gallium Indium, Alfa Aesar
[2] Sherline 4000, Sherline Products Inc

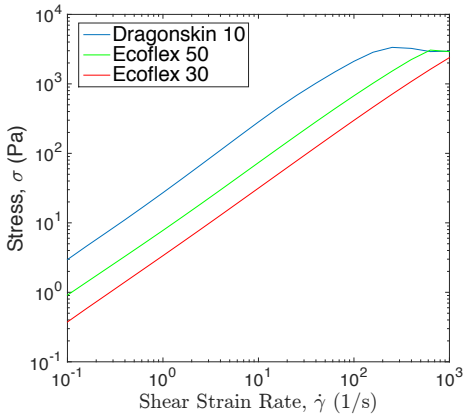

FIGURE 4.1: Stress vs. shear strain rate curves of three silicone materials measured by a rheometer.

attached to the cylinder. If we extrapolate this concept to a layer covering the entire cylinder, something similar should be expected. In previous experiments, where this concept was tested with honey on a rotating cylinder, instabilities occurred [22]. For this experiment, instabilities needed be minimized. To do this, a way to dominate the liquid-liquid interaction within the silicone substrate is necessary. This can be done by maximizing the ratio of the liquid-solid interaction between the silicone substrate and the cylinder to liquid-liquid interaction. A method of doing this is to introduce a temporal constraining solid that would bring the system to such stability. This last element can be thought of as a scraping tool, similar to a cutting tool on a lathe. The setup used will be discussed on the next section.

Experiments on the reliability of the manufactured polymer layer were performed and shown in the results section.

4.1.1.2 eGaIn Writting

One way in which our method of manufacturing is different is in the adhesion approach of eGaIn to the substrate. eGaIn develops an oxide skin which prevents it from adhering properly to its substrate. As time progresses, the oxide skin becomes thicker, which decreases the wettability [23]. In our manufacturing process, it was necessary to control the oxide skin to our needs. On one hand, the oxide skin is beneficial to keep the eGaIn from leaking from the substrate. On the other hand, the oxide skin prevents adhesion to the substrate. Our approach consisted in having 10 ml of acetone inside the syringe with the eGaIn to prevent too much oxide layer from forming. In addition, a beveled needle was used instead of a flat one, and the needle touches the substrate in the configuration shown in figure 4.2(a) and figure 4.2(b).

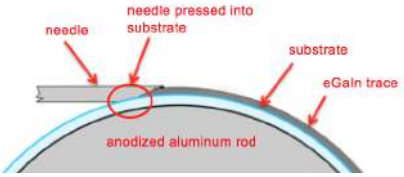

(a) Skin

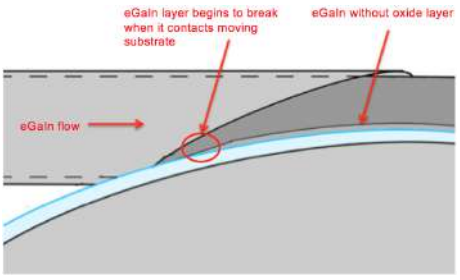

(b) Contact Forces

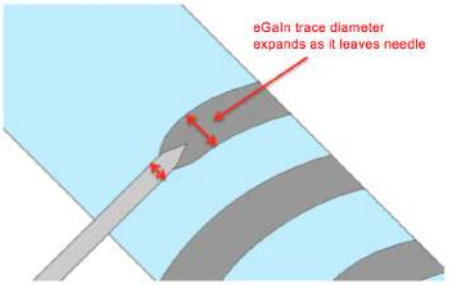

(c) Skin Closeup

FIGURE 4.2: Needle placement on substrate (a) Cross-section of sensor as eGaIn is deposited (b) Close-up view of (a), illustrating how we believe eGaIn skin breaks during manufacturing procedure. (c) Isometric view of eGaIn expanding as it leaves the needle. Obtaining a real photo proved difficult because of the speed of the writing procedure.

4.1.1.3 Covering Layer

If the method of covering the eGaIn pattern involves a smoothing tool (temporal constraining solid), just like in the first step, it is likely that the constraining solid will displace not only the silicone, but the eGaIn as well. Hence, the method of covering the pattern consists in dispensing a silicone rope in a controlled manner, so that it covers the entire surface in a helical fashion. Although theoretically this method does not provide a uniform result comparable to the first layer, it nonetheless achieves a full enclosure of the pattern. In addition, a continual rotation of the cylindrical structure prior to curing would improve the distribution. This proved to be the case, which can be observed in further sections.

The needle was placed parallel to the ground, with the opening facing towards the floor. The needle was pressed slightly into the substrate, so that the substrate partially obstructed the needle opening. This configuration aided in breaking the eGaIn oxide

layer. While the eGaIn deposits on the substrate, the oxide layer is broken by contact forces between the substrate and eGaIn induced by the rotational and translational movements of the substrate relative to the needle[3].

4.1.2 Fabrication Setup

To build our setup, we modified a 3-degree of freedom mini-lathe, which can be seen in Figure 4.3. To do this, we automated the rotational degree of freedom and an axial degree of freedom along the axis of the chuck. We did this via stepper motors[4], two stepper motor microcontrollers[5], and 1/4 in acrylic mounts machined with a laser cutter. We integrated an acrylic laser-cut smoothing tool that is engaged manually in a cross-sectional way, just like a normal lathe tool would. The smoothing tool can be seen in figure 4.4. The type of rods used to lay the polymer were precision anodized aluminum rods[6] in order to have a smooth interface with the polymer so that the sensor could easily be removed after fabrication. In addition, 3D-printed customized needle holders were built in order to dispense material. A syringe pump[7] was used to dispense eGaIn and polymer. To prevent energy storage in the system when dispensing eGaIn, we used a glass syringe[8] and flexible yet hard tubing. Before filling the syringe with eGaIn, the syringe was filled with approximately 0.4 ml of acetone.

4.1.3 Testing first layer

In order to test if the first layer of the process was robust enough to perform the rest of the manufacturing process, the metrics of eccentricity, viscosity, waviness, and thickness were compared and measured. The data is visualized in the Results section.

4.1.3.1 Eccentricity

We tested the effects of eccentricity on the aluminium rod and the polymer. The tool is a set distance away from the eccentrically rotating cylinder, which would intuitevely imply variation of thickness along the radius. It would be expected that sinusoidal variation between the rod and the polymer layer would be opposite, but it is not the case, as can be seen in figure 5.1(a). Both sinusoids would seem to be close to alignment with each

[3]Figure provided by Andrew Tallaksen
[4]3302_0 - NEMA-17 Bipolar 48mm Stepper (0.9 Step Angle), Phidgets
[5]1067_0 - PhidgetStepper Bipolar HC, Phidgets
[6]Anodized 6061 Aluminum - 1" Diameter - 6" Long, McMaster Carr
[7]ERA NE-1000 pump
[8]Hamilton GASTIGHT Number 1005

other, with the exeption of a slight slant seen in the polymer sinusoid. The slant is due to the inertial forces. In figure 5.1(b) the subtraction of both sinusoids can be seen.

4.1.3.2 Viscosity

The more viscous the polymer, the less waviness it tends to have. This is due to the cohesive forces being stronger in the more viscous liquids than the less viscous ones. The relationship can be observed in figure 5.5. Also, when viscosity is higher, the difference between the actual and theoretical thickness becomes smaller. This can be seen in figure 5.6.

4.1.3.3 Waviness

Waviness is defined as the least squares error of low frequency variations on the surface of the cured polymer. Waviness seems to increase as the theoretical thickness of the polymer is increased. As thickness becomes greater, the wake that is being smoothed out by the tool is bigger and more unstable. This causes the polymer to not be equally distributed along the circumference. Hence, some areas of polymer are farther along the radius, which causes the centrifugal force to dominate. Moreover, the polymer being smoothed out is relying mostly on cohesive forces to stay on the rod at a high thickness. This behavior can be seen in figure 5.4. If the thickness is increased over 1.143 mm, the system goes unstable.

Spindle speed does not seem to have a major effect on waviness of the polymer. This can be seen in figure 5.3.

4.1.3.4 Thickness

Thickness seems to decrease as the speed of the spindle increases. In figure 5.2 one can observe the relationship between thickness and speed.

4.1.4 Parameters for Manufacturing

To perform the experiment, the machine is set up with preset parameters. These parameters correspond to the rotational speed and axial speed of the machine. The smoothing tool is set up manually depending on the desired thickness. We found that the thickness of the polymer was not constant if we kept the ratio of axial to rotational speed the same when varying both speeds. This led us to select a set of speeds that would fall

under the capabilities of our system while giving desirable results. The preset speeds for axial and rotational speed correspond to 0.635 mm/s and 1-5 rev/s respectively. For experiments where spindle speed was held constant, 3 rev/s was selected as the speed for all experiments because it was the fastest speed that was safe for long term operation of our machine. Theoretical thickness is referred to the thickness set by the scrapper. The real thickness is the thickness measured after the polymer cures. Speed, theoretical thickness, and viscosity are the parameters that most affect the real thickness. After presetting the values of the machine, we prepare the polymer to be used. We turn on the machine and manually poor the polymer material on top of the rod after the tool so it can engage the material. Once we have poured enough material, we make sure the tool performs one pass, and then we disengage the tool. Depending on the thickness set, we let the polymer cure for a certain amount of time. For Ecoflex and Dragonskin, time ranges from an hour to two for curing.

The rate of flow of the eGaIn is dependent on the diameter of the needle, the diameter of the plunger, the diameter of the syringe, and the velocity of the plunger inside of the syringe. After programming the pump to move at a velocity that correlates to the desired output, the pump did not produce an even and continuous coil on the sensor, often producing bubbles along the trace. We suspect this is because of the eGaIn's wetting properties on the substrate. The calculations for coil size assumed a perfectly circular cross-section of the coil, but this is not what is produced because eGaIn is not perfectly wetting under these conditions. The shape that the cross-sectional coil assumed may have required less eGaIn than what was initially calculated. In addition, we suspect that the diameter of the eGaIn cross-section increases as it leaves the pressured environment of the needle into the less pressured lab atmosphere, shown in figure 4.2, consistent with Bernoulli's principle [24].

To compensate for the inconsistencies in the eGaIn writing procedure created by the wetting and diameter increase upon exiting the needle, we added a scaling factor to the syringe speed. This produced a smaller output of eGaIn to limit bubbles. The scaling factor varied based on the sensor diameter.

eGaIn also does not behave like a Newtonian fluid. It reacts as an elastic material until it reaches an applied critical surface stress (0.5 N/m) [18]. When the pump is first turned on, a puddle of eGaIn forms on the substrate after the eGaIn overcomes the applied critical surface stress. This is corrected by wiping off the puddle with a paper towel and isopropanol. The applied critical surface stress is a limiting factor when tuning the scaling factor mentioned above. If the scaling factor is too small, discontinuities appear because the pressure from the syringe is not enough to overcome the applied critical surface stress.

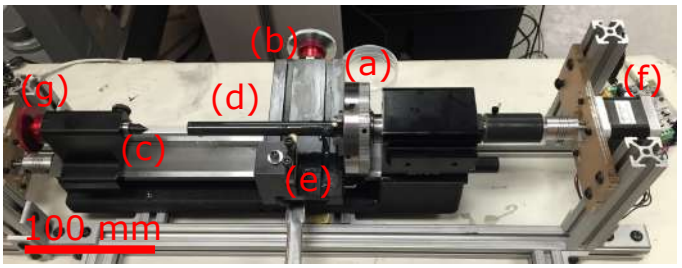

FIGURE 4.3: Smooth Cylindrical Coater. The device is a modified Sherline Mini lathe. (a) Spindle. (b) Manual Cross-sectional degree of freedom. (c) Live center. (d) Aluminum Rod. (e) Smoothing tool. (f) Stepper motor with laser-cut mount, which provides power to the spindle. (g) An automated axial degree of freedom to move the stage along the axis of the spindle.

4.1.5 Fabrication Process

The fabrication process starts by manually pouring polymer on a rotating anodized aluminum rod. This polymer is then smoothed out by a tool attached to the lathe. The process of the tool smoothing the polymer can be seen in figure 4.4. This process is analogous to how a lathe would remove solid material but in this case the tool removes a fluid. After the fluid is smoothed out, the lathe continues to rotate, so that a uniform coat forms. The lathe then spins for an hour until the substrate is cured.

Once this process is complete, the syringe pump is used to write a helical pattern on the substrate via a beveled needle, as previously described.

After the pattern is written, polymer is prepared and dispensed in a controlled manner on top of the pattern, once again, via a syringe pump and a 25 gage flat needle. The axial and radial speeds of the lathe are matched to those of the pump in order to cover the entire surface with a spiral of substrate. This provides a final covering layer for the sensor. This process can be seen in figure 4.6. The cross-section of the final sensor can be seen in figure 4.9.

36-AWG copper wires were used as lead wires for the sensor. The sensor displayed significant hysteresis in early testing due to the poor interface between the copper wire, eGaIn, and silicone. To mitigate the hysteresis, compliance matching principles were used. To optimize this matching, the area of interface needed to be bendable yet not stretchable. Hence, scotch tape[9] was wrapped halfway around the top and bottom of the sensor. Bonding of the tape was enhanced with Sil-Poxy[10]. This feature improved the reliability of the interface, significantly reducing hysteresis in later tests.

[9] 3M Scotch Magic, 3/4”x300”,1” core
[10] Smooth-on, Silicone Rubber Adhesive

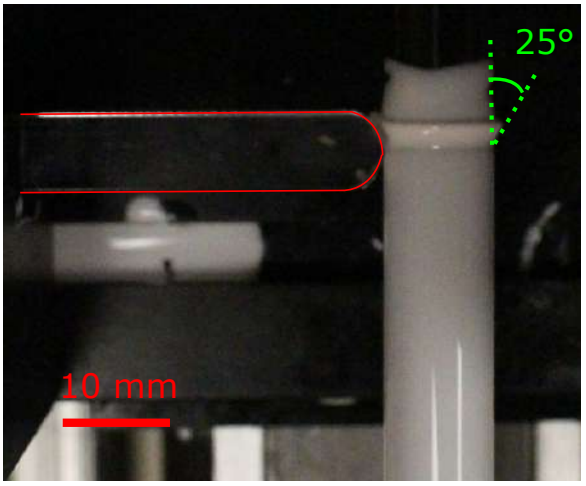

FIGURE 4.4: Smoothing Tool Engaging Polymer. This tool is positioned at a determined distance from the rod and controlled with the autonomous degree of freedom in order to achieve a uniform polymer layer. The tool is highlighted in red, and the angle of the wake of the polymer is highlighted in green.

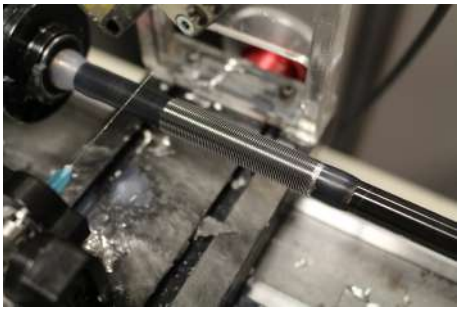

FIGURE 4.5: 14.17 coils/cm pattern writing.

FIGURE 4.6: Covering pattern with new layer of silicone via controlled silicone deposition.

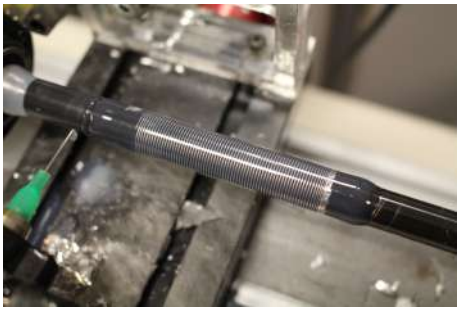

FIGURE 4.7: Pattern covered with new layer of silicone.

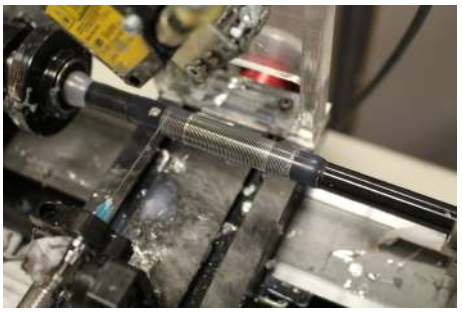

FIGURE 4.8: 14.17 coils/cm multilayer pattern writing.

FIGURE 4.9: Cross-section of the Sensor. The resulting cross-section shape of the eGaIn pattern is approximately semicircular.

4.2 Sensor Characterization

4.2.1 Theoretical Modeling

The sensor operates on the principle that its deformation locally matches that of the body onto which it is applied. In the following examples, the sensor is applied to a soft-body cylinder, which only undergoes deformations that maintain it's shape as a strict cylinder. Therefore, the eGaIn coil will always maintain the geometry of a cylindrical helix.

The three modes of cylindrical deformation are axial, radial, and torsional, which directly correspond to changes in the sensor length, radius, and angle of wrap, respectively. These parameters are given as l, r, and θ, respectively. Alternative but equivalent parameters include helix angle, number of turns, pitch, and diameter[11].

The total arc length, s, of the helix is parameterized as:

$$s = \sqrt{\theta^2 r^2 + l^2} \tag{4.1}$$

The sensor deformation is transduced by applying the following model as mapping between measured resistance and deformation. The resistance along a wire of length s with resistivity ρ is given by:

$$R = \frac{\rho s}{A} \tag{4.2}$$

Because a cylindrical helix geometry is maintained, we can assume a constant cross-section area. Also assuming incompressibility of the eGaIn, i.e. constant volume, V, we can conclude that any measured change is due to a change in the helix arc length. We can now write the resistance as:

$$R = \frac{\rho s^2}{V} = \underbrace{\frac{\rho}{V}}_{\text{constant}} \left(\theta^2 r^2 + l^2\right) \tag{4.3}$$

Clearly, the sensor resistance is quadratic with respect to any of the three parameters, and thus any change in resistance will be realized as a linear combination of the three parameters, given by the gradient:

[11] Theoretical Model Provided by Jonathan King

$$\nabla R = \frac{\rho}{V}\left(\frac{\partial R}{\partial \theta}\mathbf{e}_\theta + \frac{\partial R}{\partial r}\mathbf{e}_r + \frac{\partial R}{\partial l}\mathbf{e}_l\right)$$
$$= \frac{\rho}{V}\left(\left(2\theta^2 r + l^2\right)\mathbf{e}_\theta + \left(2\theta r^2 + l^2\right)\mathbf{e}_r + \left(\theta^2 r^2 + 2l\right)\mathbf{e}_l\right) \quad (4.4)$$

4.2.2 Testing of Cylindrical Modes

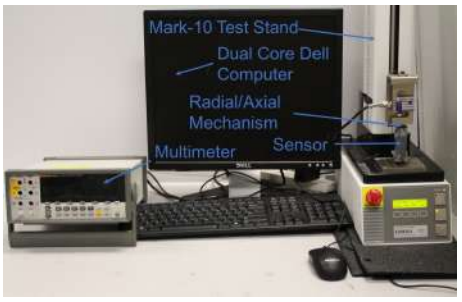

FIGURE 4.10: Experimental Setup used to test Sensor.

The sensor was tested in the 3 modes of cylindrical coordinates. To do this, radial, axial, and rotational setups were built.

A radial testing mechanism was used to expand the sensor in a controlled manner. The mechanism can be seen in figure 4.11. The mechanism consists of six radially arranged six-bar mechanisms to convert axial motion to radial motion. As the mechanism was compressed, the arms moved out radially to expand the sensor wrapped around the mechanism. The mechanism was 3-D-printed. We tested for 3 sensors, as the mechanism could not be further miniaturized given our equipment. In order to map change in resistance to change in radius, the experimental setup in figure 4.10 is used. The cylinder is expanded for a range of 1 cm. The results can be seen in figure 5.8. We mapped the linear distance of the Mark-10 to the radial distance of the mechanism using a caliper[12]. Due to inherent tolerance restrictions in 3-D printing of the mechanism, a curve was fit to the data instead of using kinematic first principles. Then, the L_2 norm was used to derive the uncertainty of data, which was of 1 mm. The data shows low hysteresis due to the low thickness of the substrate.

The axial testing mechanism was also 3-D-printed. A model of it is shown in figure 4.12. Results of the tests using this mechanism can be seen in figure 5.9.

For torsion, a highly bendable polymer tube was clamped to the experimental setup previously mentioned. An angle finder was attached to the end of the rod as seen in

[12]Mitutoyo Digital Caliper, MF#500-196-30

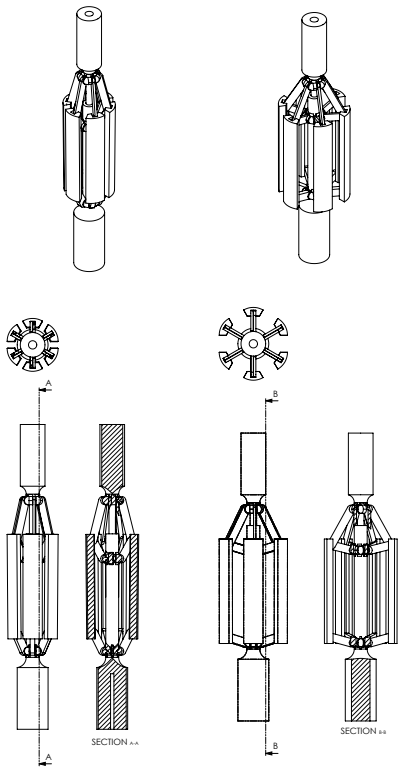

FIGURE 4.11: Radial Characterization Mechanism. A radial testing mechanism was developed to test the sensor. The mechanism expands radially as pushed axially. The mechanism consists of 6 prongs that expand and approximately keep a circular configuration. Each of the prongs expands by means of a 6-bar mechanism.

figure 4.13. The experiments ranged 180 degrees, providing controlled torsion the rod in both directions. The results can be seen in figure 5.10.

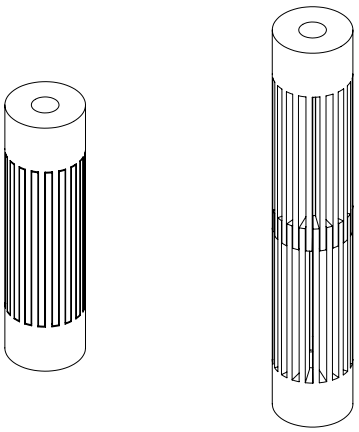

FIGURE 4.12: Axial Characterization Mechanism. An axial testing mechanism was developed to test the sensor. The mechanism expands axially. The mechanism consists of two cylindrical structures with prongs which fit into each other. This allows for consistent diameter of sensor while expanding. Oil is used to lubricate the mechanism in order to prevent friction.

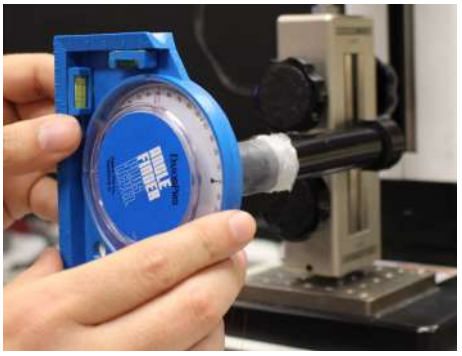

FIGURE 4.13: Torsion Characterization. Torsion Experimental Setup. Sensor is placed closer to the angle finder for these results. When sensor is placed in the center, only an extra sensitivity of 0.02 Ω is obtained. See 5.10 for results.

4.3 Characterization of Sensor-PAM Package

4.3.1 Sensors Used in Package

Previously, a 3-D helical soft sensor was manufactured through using multiple-layer casting and a low-friction thread for embedding a helical microchannel in an elastic bladder [17]. The low-friction thread would then be removed and a liquid conductor (e.g. eutectic gallium-indium, EGaIn [18]) would be injected in the channel. Some limiting factors of this process are: the diameter of the low-friction fiber, the angle limit for the fiber to be pulled out, and how thick the polymer layer should be. Our sensor was designed to overcome some of these challenges. It is a hollow cylinder with an EGaIn[13] helical pattern as seen in Fig. 4.14 just like in the previous method. A

[13]Eutectic Gallium Indium, Alfa Aesar

FIGURE 4.14: Soft Sensor Prototype.

modified mini-lathe[14] with two automated DOFs was used to manufacture the sensor. There is a three step process for the manufacturing process. First, silicone rubber[15] is poured on a rotating cylindrical surface and smoothed out with a smoothing tool, analogous with a cutting tool on a regular lathe. Then, a liquid metal high-density helical pattern is written on top of the cured silicone layer with a syringe pump[16]. The final step consists in adding another layer of silicone on the pattern while rotating, again with the syringe pump, in order to preserve the pattern. The process is controlled via a MATLAB program. The coil density, length, and diameter of the coil can be specified in the program. We fabricated two sensors for purposes of characterization. One sensor had 14 coils/cm and the other 9 coils/cm. The total length of both coils was about 2.54 cm.

4.3.2 Muscle Used for Package

The implementation of PAMs has been, for the most part, divided into two camps. The first, containing the majority of PAM users, use very cheap and imprecise designs that allow for easy prototyping and concept testing. The other camp uses PAMs for precision applications in industry, requiring more reliable and accurate PAMs. The drawback of this approach is that there are few manufacturers, i.e. FESTO[17], with long lead-times and relatively high costs.

The design method presented provides a cost-effective solution for increased PAM life-time, precision, and quality.

The PAM consists of an elastomeric bladder inside of an expandable braided sleeve. However, unlike most PAM designs, the bladder and sleeve are fabricated as a single unit. The ends replace the common zip tie seals with swaged brass ferrules and end-fittings that allow for a variety of air inlet options and mechanical interfacing such as rod ends and ball joints. The assembly and details of this design are shown in Fig. 4.15.

[14] Sherline 4000, Sherline Products Inc
[15] Dragonskin 10, Smooth-On, Inc
[16] ERA-1000 Syringe Pump, Pump Systems Inc
[17] FESTO, Fluidic Muscle DMSP/MAS

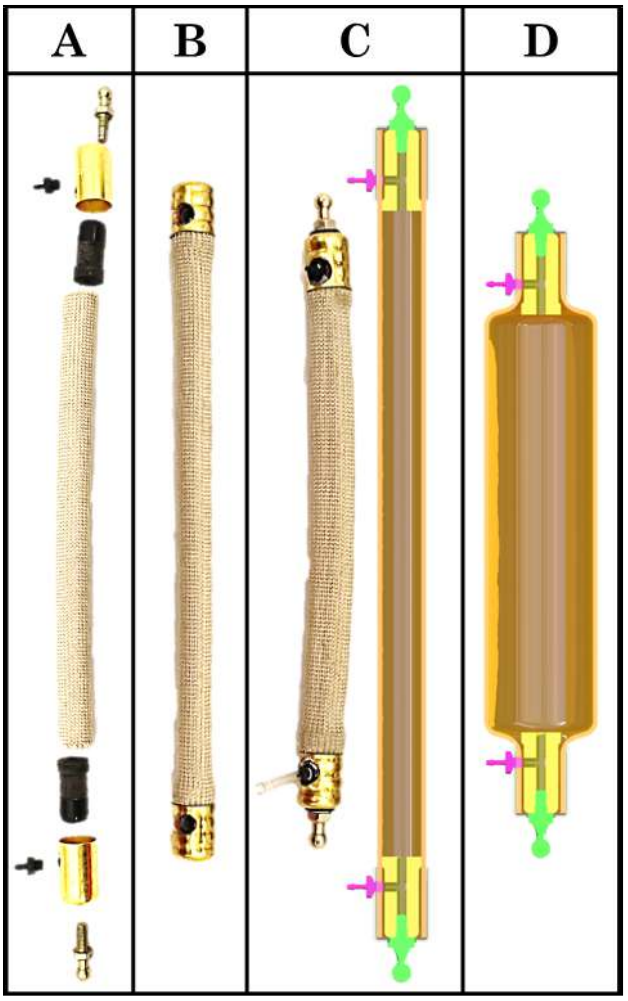

FIGURE 4.15: PAM design and assembly detail: (A) Individual components; The muscle tube, inserts, ferrules, fittings and ball joints. (B) PAM after the inserts have been fit and the ferrules swaged and drilled. (C) Final PAM with fittings and ball joints & CAD cross-section for detail. (D) CAD cross-section of the inflated PAM.

For muscles utilizing the integrated sensor, the sensing device should be fitted over the muscle tube between steps A and B of the PAM assembly.

The result is a PAM that has higher pressure and force limits, improved fatigue life, precision mechanical interfacing, and repeatable manufacturing[18].

4.3.3 Circuit

An Arduino Uno[19] with an 8-bit microcontroller (Atmel ATmega328) was used to read sensor data and regulate PAM air pressure for closed-loop control. The sensor interface circuit shown in Fig. 4.16 drives the sense coil, R_{Sensor}, with a small fixed current. The

[18]Muscle design and assembly process created by Jonathan King
[19] Arduino Uno, Arduino

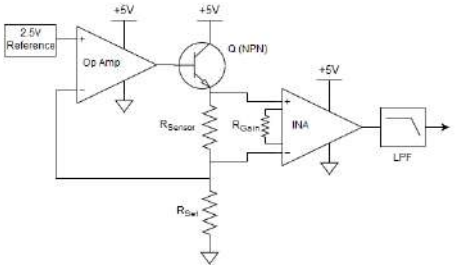

FIGURE 4.16: Circuit used for feedback and actuation of the system.

Op Amp (Linear LT1077) maintains the preset reference voltage across R_{Set}, via transistor Q (2N3904). This fixes the current through R_{Set}, and R_{Sensor}. The Instrumentation Amplifier (INA, Analog Devices AD8226) amplifies the small voltage across R_{Sensor} to a range within the input limits of the microcontroller's ADC. A 1kHz single pole RC filter is used to prevent aliasing. The 2.5 V reference was implemented with a voltage divider.

4.4 Sensor-PAM Package Modeling

The braided fibers composing the PAM sheath and the EGaIn microchannel spanning the integrated sensor have a circular-helix shape. A helix can be defined by its axial-length (l), diameter (d), and number of coils (n), related by the arc-length (s) with the expression:

$$s^2 = l^2 + (\pi n d)^2 \tag{4.5}$$

For the PAM, the fibers are assumed to be inextensible, leaving s_m and n_m constant. For a relative contraction of axial length, there will be a relative expansion in diameter. The strains, ϵ_{l_m} and ϵ_{d_m} are related by:

$$\begin{aligned} \epsilon_{d_m} &= \frac{\sqrt{s_m^2 - (\epsilon_{l_m} l_{m_i} + l_{m_i})^2}}{\pi n_m d_{m_i}} - 1 \\ &= \sqrt{1 - \alpha_m^2 \epsilon_{l_m} (2 + \epsilon_{l_m})/(\pi n_m)^2} - 1 \end{aligned} \tag{4.6}$$

Where the measured initial values define the PAM aspect ratio, $\alpha_m = l_{m_i}/d_{m_i}$, and s_m is replaced using (4.5). Length and Diameter strains were measured and compared to the model with results in Fig. 5.11.

The expression for sensor resistance is: $R_s = \rho s_s / A_s$, where ρ is the EGain resistivity. The sensor design prevents slip along the PAM during contraction, thus the axial-length and diameter strains are equivalent for the PAM and sensor. Approximating the EGaIn fluid as incompressible we can define a constant volume given by the product of the channel arc-length and cross-sectional area, $V = s_s A_s$. This reduces the resistance expression to $R_s = \rho s_s^2 / V$. We can now relate the relative change in resistance from the initial measured state, $\epsilon_{R_s} = \Delta R_s / R_{s_i}$, to the PAM strain:

$$\begin{aligned} \epsilon_{R_s} &= \frac{\rho s_s^2 / V}{\rho s_{s_i}^2 / V} - 1 \\ &= \frac{(1+\epsilon_{l_m})^2 l_{s_i}^2 + (\pi n_s (1+\epsilon_{d_m}) d_{s_i})^2}{l_{s_i}^2 + (\pi n_s d_{s_i})^2} - 1 \end{aligned} \tag{4.7}$$

Defining the sensor aspect ratio, $\alpha_s = l_{s_i} / d_{s_i}$, and the ratio of coils in the PAM and sensor helices, $\kappa_c = n_m / n_s$. Used together with (4.6), the resistance change reduces to:

$$\begin{aligned} \epsilon_{R_s} &= \underbrace{\frac{(\alpha_s \kappa_c)^2 - \alpha_m^2}{(\alpha_s \kappa_c)^2 + (\pi n_m)^2}}_{\text{constant} \rightarrow c_{sm}} \left(\epsilon_{l_m}^2 + 2\epsilon_{l_m}\right) \\ &= c_{sm} \epsilon_{l_m} (\epsilon_{l_m} + 2) \end{aligned} \tag{4.8}$$

Thus, the relative change in resistance is quadratically proportional to the relative change in the PAM length[20].

4.5 Characterization of Sensor-PAM Package

4.5.1 Experimental setup.

The Experimental setup consists of a motorized test stand[21], air supply, a XPH 35-4D Dual DC Sorensen power supply, an arduino uno board, NI LABView 2010, a National Instruments DAQ, one PAM which ends are coupled to the test stand, a 14 coils/cm soft sensor, a 9 coils/cm soft sensor, and four 1.4 N/mm spring connected in parallel interfaced in series with the muscle.

[20] Modeling Provided by Jonathan King
[21] Mark-10 Motorized Test Stand ESM301

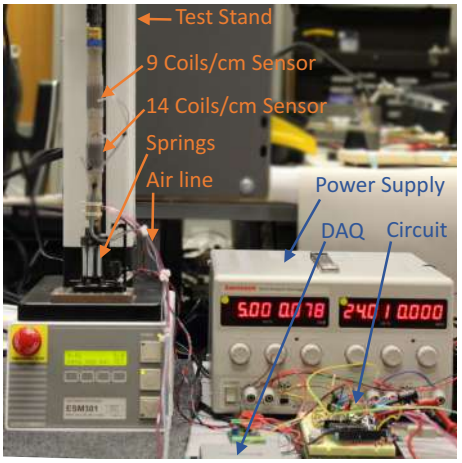

FIGURE 4.17: Experimental setup for characterization of two sensors with muscle contraction.

4.5.2 Procedure

First, the muscle was attached in series to the Mark-10 with a spring, and the sensors were connected with the specified circuit in Fig. 4.16. Then, the Mark-10 was setup to an initial length corresponding to the length of the muscle plus the length of the spring. After this, the muscle was connected to the air supply, and the following were measured: Load cell force F muscle length l_m, muscle diameter d_m, sensor 1 resistance R_{14}, sensor 2 resistance R_9, and gage pressure p_g. At this point, the Mark-10 was lowered, recording at least 10 readings total for each variable, until maximum contraction was reached. Data was also recorder while the Mark-10 was brought up until initial length of the muscle is reached, again, taking atleast 10 measurements for every variable.

The evaluated data is shown in Fig. 5.12 and Fig. 5.13. The correlation is very remarkable; a comparison of the model parameters from (4.8) with best-fit parameters in Table 4.1 effectively validates the characterization. It should be noted that because the measurements were taken for both loading and de-loading of the PAM, and little to no hysteresis was observed, that the sensor-length relationship is bidirectional. Thus, the sensor is a viable candidate for use in feedback control.

TABLE 4.1: Characterization parameters.

	9 coils/cm		**14 coils/cm**	
	Theory	**Best**	**Theory**	**Best**
c_{sm}	-2.1959	-2.1653	-2.1972	-2.1647
R^2	0.9931	0.9938	0.9975	0.9983

Following characterization (4.8) can be restated with Δl_m as the dependent variable for implementation in the controller:

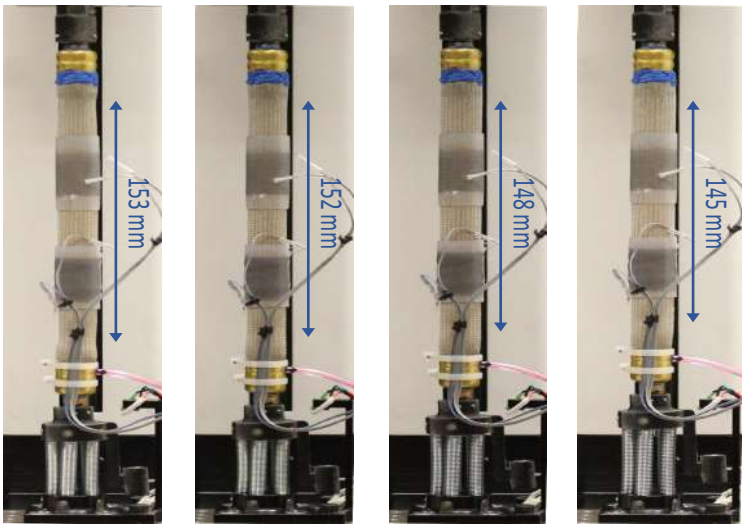

(a) (b) (c) (d)

FIGURE 4.18: (a) Deflated PAM. (b) Inflated PAM at 69.0 kPa. (c) Inflated PAM at 137.9 kPa. (d) Inflated PAM at 206.8 kPa.

$$\Delta l_m(\Delta R_s) = l_{m_i}\left(\sqrt{\frac{\Delta R_s}{c_{sm}R_{s_i}} + 1} - 1\right) \tag{4.9}$$

4.6 Control

An Arduino microcontroller[19] was used to control two valves[22] at 30 Hz for inflow and outflow of the PAM. Due to the high frequency response of the valves and lack of inertia, sliding mode was applied to the system.

4.6.1 Experimental Setup for Control

4.6.2 Control Derivation

The following state space model was used to prove the stability of the system:

$$\dot{x}_1 = x_2 \tag{4.10a}$$

$$\dot{x}_2 = \frac{\bar{C}}{M}x_2 + \frac{\bar{K}}{M}x_1 \tag{4.10b}$$

[22] 24V X-Valves, Parker Inc

Where x_1 and x_2 are position and velocity, with $\dot{x}_1$ and $\dot{x}_2$ are their time derivatives respectively. Position and velocity are bounded: $\mathbf{x} \triangleq [x_1\ x_2]^T$, and $\mathbf{x} \in L_\infty$. $\bar{C}$ and $\bar{K}$ are upper bounds of the damping and spring coefficients of the system, and M is the total mass.

$$\frac{\bar{C}}{M}x_2 + \frac{\bar{K}}{M}x_1 = 0 \tag{4.11}$$

By solving (4.11), we arrive to (4.12a) and (4.12b), which shows that $\mathbf{x} \to 0$ as $t \to \infty$.

$$x_1(t) = x(0)e^{-\frac{\bar{K}}{\bar{C}}t} \tag{4.12a}$$

$$x_2(t) = -\frac{\bar{K}}{\bar{C}}x(0)e^{-\frac{\bar{K}}{\bar{C}}t} \tag{4.12b}$$

To improve the system's response convergence to stability and tracking, a low level digital controller is implemented. To do this, a control input is added to (4.10b), resulting in the state space of (4.13a) and (4.13b).

$$\dot{x}_1 = x_2 \tag{4.13a}$$

$$\dot{x}_2 = \frac{\bar{C}}{M}x_2 + \frac{\bar{K}}{M}x_1 + u \tag{4.13b}$$

We design the commonly used sliding manifold σ:

$$\sigma \triangleq \dot{e} + \alpha e; \quad \alpha \in \mathbb{R}_{>0} \tag{4.14}$$

And design the control law, seen in (4.15).

$$u \triangleq K_s(\sigma) \tag{4.15}$$

where $K_s > 0$, and is a designed sliding mode gain.

Then, we do Lyapunov analysis to prove the stability of the controller, where we select positive definite lypunov function shown in (4.16).

$$V \triangleq \frac{1}{2}\sigma^2 \tag{4.16}$$

and its time derivative is found and simplified in (4.17).

$$\begin{aligned}\dot{V} &= \sigma\left(\underbrace{\frac{\bar{C}}{M}x_2 + \frac{\bar{K}}{M}x_1 + \frac{\bar{K}}{\bar{C}}x_2}_{W(x_1,x_2)} + u\right) \\ &= \sigma W(x_1, x_2) + \sigma(\sigma)\end{aligned} \tag{4.17}$$

We define constant $L \geq W(x_1, x_2)$. As we know the mass of the system, the upper limits of our stiffness and damping coefficients, and that x_1 and x_2 are bounded.

$$(\sigma) = \frac{|\sigma|}{\sigma} \tag{4.18}$$

We use (4.18) to upper bound the lyapunov. See (4.19).

$$\dot{V} \leq |\sigma|\,(L - K_s) \tag{4.19}$$

We assume that K_s will always dominate upper bound L. We will use positive variable $\bar{\beta}$ for simplicity. See (4.20).

$$\bar{\beta} \triangleq K_s - L \tag{4.20}$$

Using the sliding mode existence condition (4.21) from [25], which turns into (4.22), the asymptotic stability of the controller is proven. From this, our gain requirement (4.23) is selected. In so far as this gain requirement is satisfied and actuators used have infinite frequency, we can guarantee global asymptotic stability for our system. In practice, infinite frequency is not possible, but with high enough frequency response can be desirable.

$$\dot{V} \leq -\bar{\beta} V^{1/2} \tag{4.21}$$

$$\sigma\dot{\sigma} \leq -\frac{\bar{\beta}}{\sqrt{2}}|\sigma| \tag{4.22}$$

$$K_s = L + \frac{\bar{\beta}}{\sqrt{2}} \tag{4.23}$$

The controller block diagram is shown in Fig. 4.19.

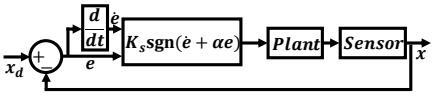

FIGURE 4.19: Controller block diagram.

Since the characterization of both sensors were very similar, we only used the 14 coils/cm version for feedback. When experimenting with the control, α from (4.14) was set to a large value so it would dominate the velocity term. We did this to avoid the effects of the degrading signal of $\dot{e}$ due to the derivative. In future work, we will implement a nonlinear observer or output feedback in order to obtain a better response. Tracking control is shown to a reference point, a square wave, and a sinusoid in Figs. 5.14, 5.15, and 5.16 respectively.

4.7 Additional Applications

In addition to the 3 modes tested, and the sensor-PAM package the sensors were briefly tested for additional applications. Strain gages can measure small deformations, yet, when deformations are large, there is no practical way of accurately sensing change. Presented are four applications in which the sensor could be used: Measuring the length of a workout stretch-band, tracking finger-bending, tracking the curvature of the backbone of a soft robot, and pressure sensing with a rigid load cell as ground truth.

For the stretch band, a multilayered sensor was used. The setup and results can be seen in figures 4.20 and 5.17 respectively. It can be seen that for a length of 50 mm of displacement, both sensor layers can track with repeatability and a resistance range of 2 Ω.

For the finger test shown in figure 4.21, repeatibility was more difficult to show because of limitations of our setup. Nevertheless, a consistent trend is shown. The results can be seen in figure 5.18.

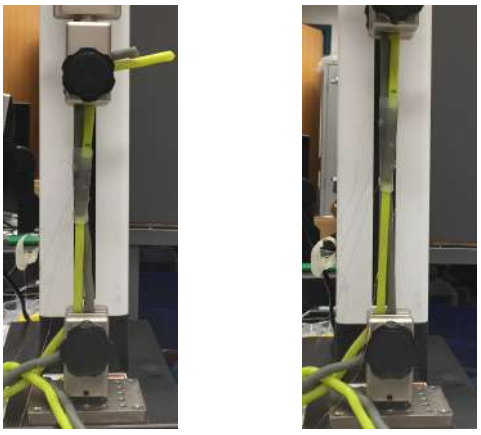

(a) Unstretched. (b) Stretched.

FIGURE 4.20: Stretchband Test.

For the backbone test shown in figure 4.22, again, repeatibility was more difficult because of the setup but a consistent trend is shown. The results can be seen in figure 5.19

In the load cell test, seen in figure 4.23, the voltage pattern is compared with the force output of the load cell. It can be seen that there is proportionality and correlation between both sensors. The reason for the difference in magnitude in the different peaks is because the sensor measures pressure and not force, and since the area with which the finger presses the load cell varies, there is flattening, especially in the intermediate peaks when pressing at high frequencies. The results can be seen in figure 4.23.

(a) Sensor on stretched finger.

(b) Sensor on bent finger.

FIGURE 4.21: Demonstration of Operation of a Sensor in Finger.

(a)

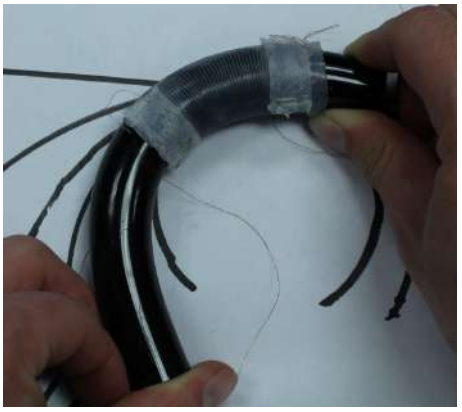

(b)

FIGURE 4.22: Backbone Test. (a) Small curvature. (b) High curvature.

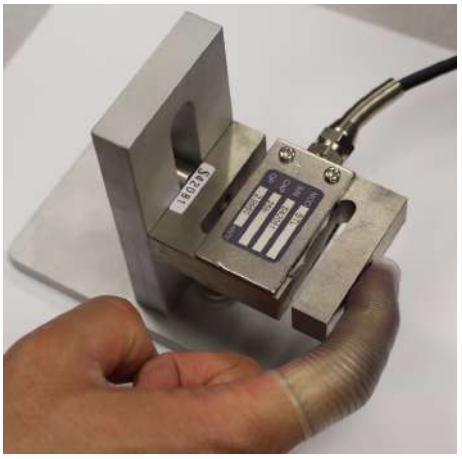

FIGURE 4.23: Load Cell Test. The Load cell is used as a proportionality ground-truth for the soft sensor signal.

Chapter 5

RESULTS

5.1 Manufacturing Results

5.1.1 Behavior of Polymer on Cylindrical Structure

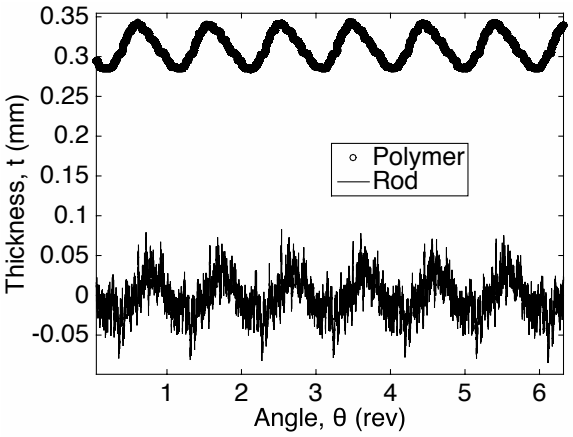

(a)

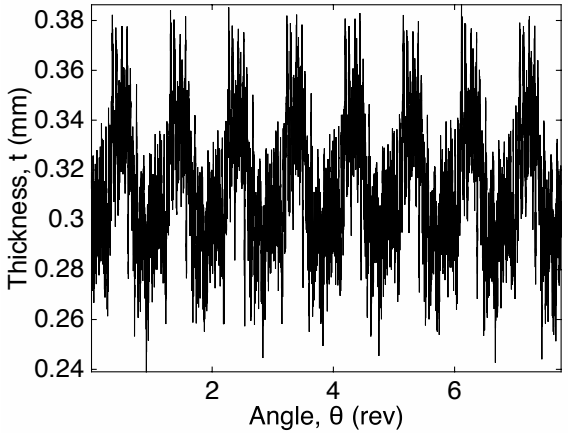

(b)

FIGURE 5.1: Eccentricity of the rod and polymer. The eccentricity of the rod and the polymer follow the same pattern. (a) Cross-Sectional Sensing of Rod and Polymer. (b) Thickness of Polymer Considering the Effects of Eccentricity.

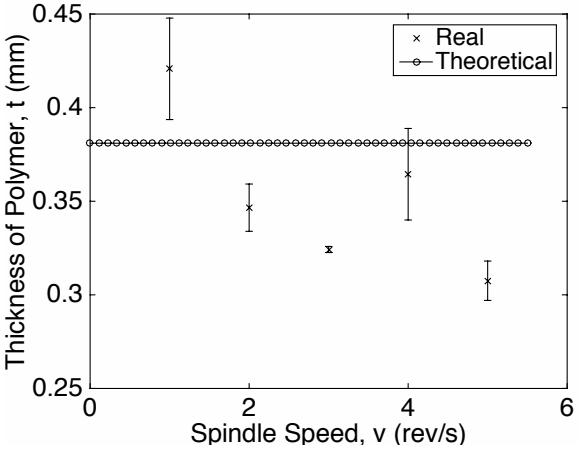

FIGURE 5.2: Thickness vs Speed. As speed increases, thickness decreases. This is due to the tool having more time per axial unit to collect material.

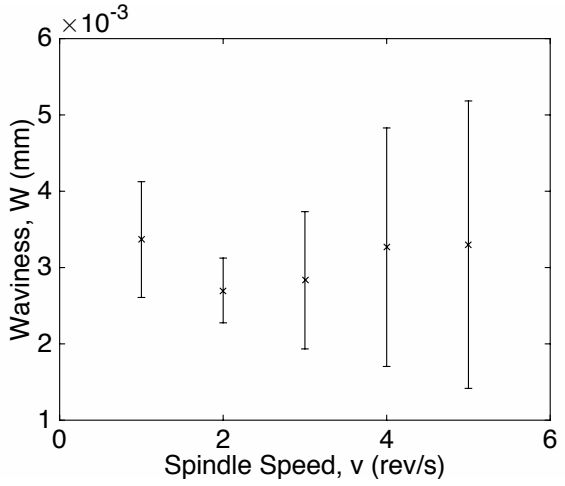

FIGURE 5.3: Waviness vs Spindle Speed. As the speed of the spindle increases relative to the axial speed, waviness remains constant. This was tested with a theoretical thickness of 0.381 mm

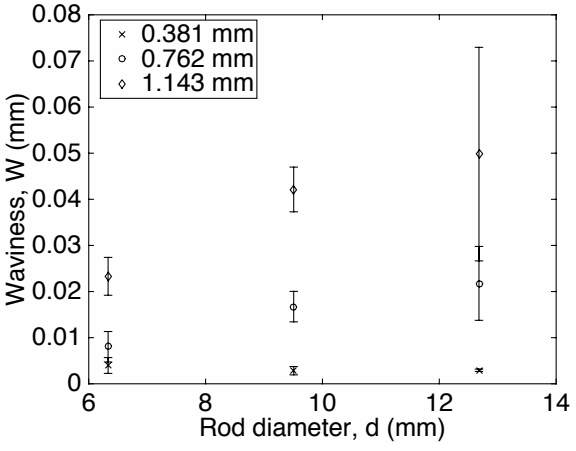

FIGURE 5.4: Waviness vs Diameter. As rod diameter increases, waviness also slightly increases, except for the 0.381 mm thickness case.

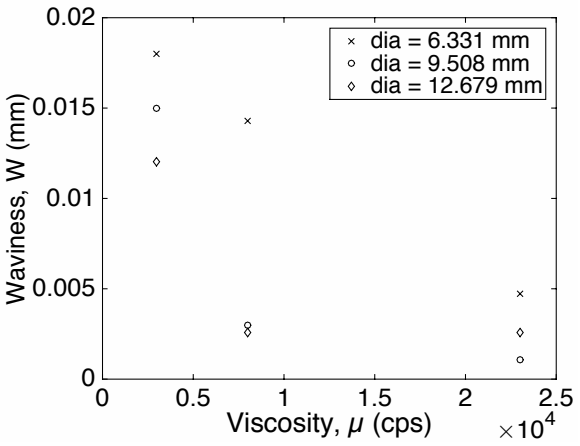

FIGURE 5.5: Waviness vs Viscosity. As rod diameter increases, waviness slightly increases for larger thicknesses. For the 0.381 mm case, waviness remained constant throughout the different diameters.

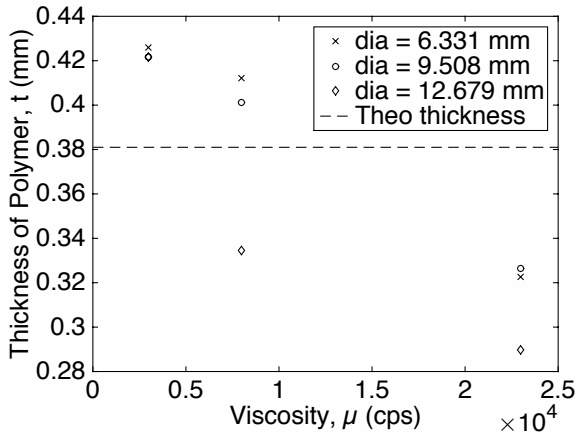

FIGURE 5.6: Thickness vs Viscosity. These samples were taken at a spindle speed of 3 rev/sec and axial speed of 0.635 mm/s. As viscosity increases, real thickness decreases.

5.1.2 Final Results of the Process

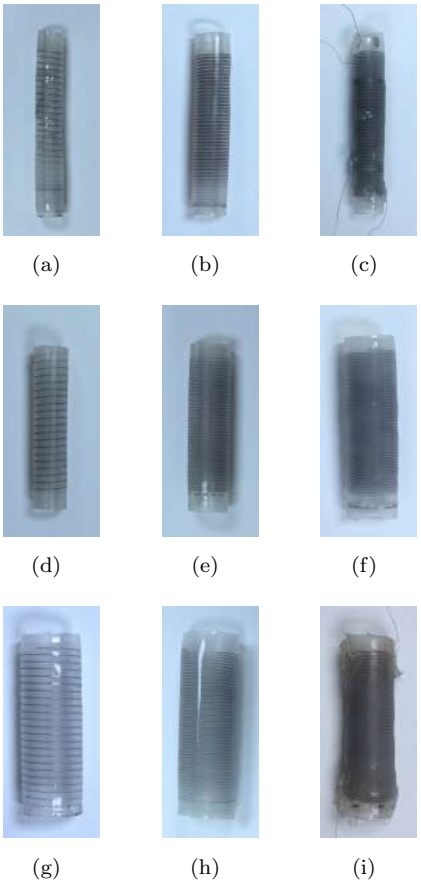

(a) (b) (c)

(d) (e) (f)

(g) (h) (i)

FIGURE 5.7: Sensors of 3 different diameters and 3 different coil densities and a 2 layer sensor. (a) Small diameter with 4.72 coils/cm. (b) Small diameter with 9.45 coils/cm. (c) 2 layer sensor of small diameter with 14.17 coils/cm. (d) Medium diameter with 4.72 coils/cm. (e) Medium diameter with 9.45 coils/cm. (f) Medium diameter with 14.17 coils/cm. (g) Large diameter with 4.72 coils/cm. (h) Large diameter with 9.45 coils/cm. (i) Large diameter with 14.17 coils/cm.

5.2 Characterization Data

5.2.1 Characterization Data of Three Cylindrical Coordinate Modes

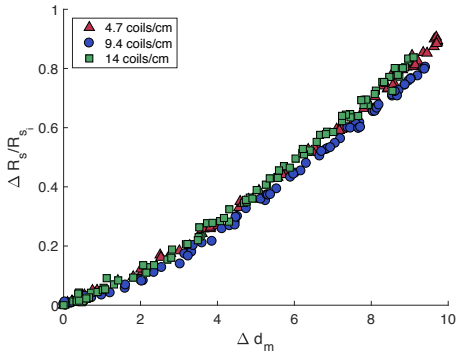

FIGURE 5.8: Resistance vs Radial Expansion. The graph shows 3 sensors of the same diameter, between 3 and 6 cm long, expanded radially using the setup in figure 4.10 and the mechanism in figure 4.11

.

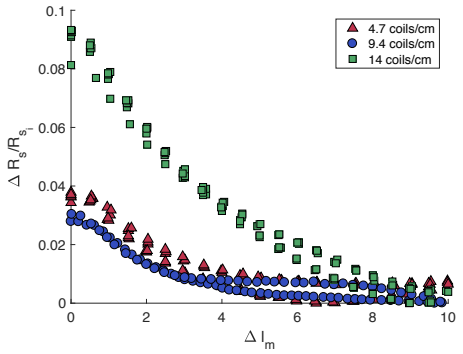

FIGURE 5.9: Resistance vs Axial Expansion. The graph shows 3 sensors of the same diameter, between 3 and 6 cm long, expanded axially using the setup in figure 4.10 and the mechanism in figure 4.12

.

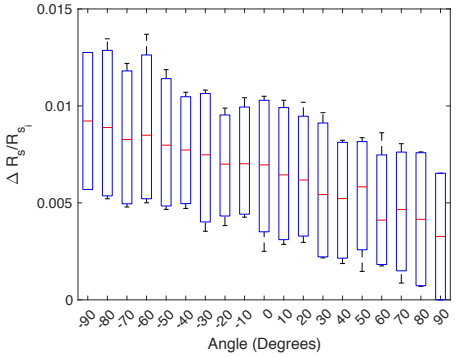

FIGURE 5.10: Torsion Characterization Results. Resistance vs Torsion Angle. Relative to the radial mode, there is a small change in torsion. Even when placing the sensor at the send of the rod, minimal readings can be captured.

5.2.2 Characterization Data of Sensor-PAM Package

The following are the characterization of two manufactured sensors tested on PAMs using the theoretical model of the muscles aforementioned:

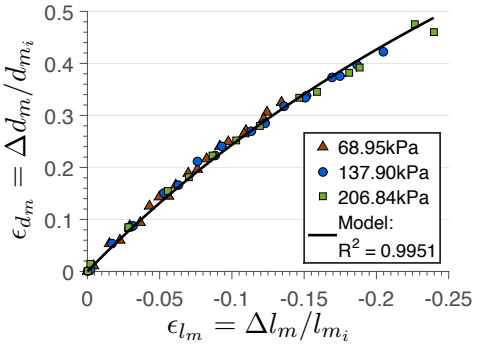

FIGURE 5.11: Relative change in length vs. distance.

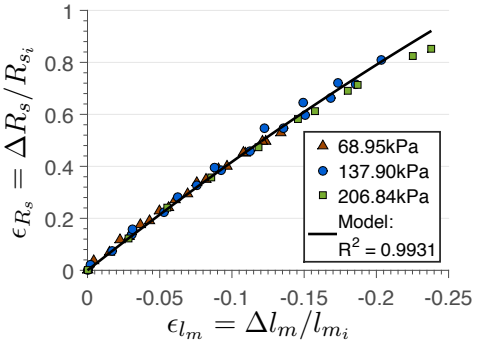

FIGURE 5.12: Sensor Characterization Results Showing Relative Change in Length vs. Resistance.

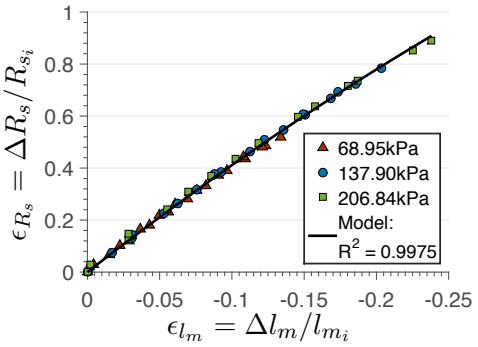

FIGURE 5.13: Sensor Characterization Results Showing Relative Change in Length vs. Resistance.

5.3 Control Data

The rise time for our range was of at most 1.071 s, and the settling time was at most 0.2 s, with overshoot not larger than the ultimate bound.

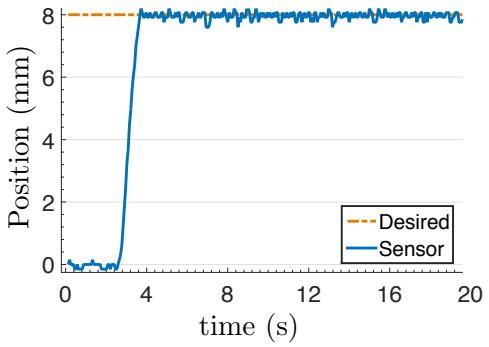

FIGURE 5.14: Tracking control with 8 mm reference using 14 coils/cm sensor.

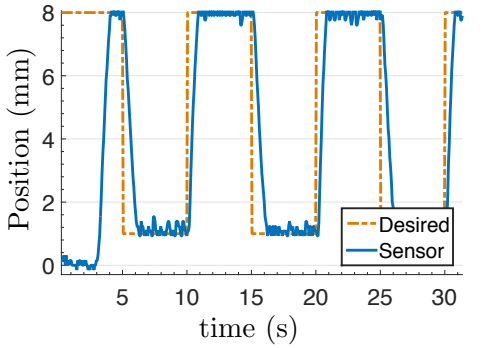

FIGURE 5.15: Square-wave tracking using 14 coils/cm sensor.

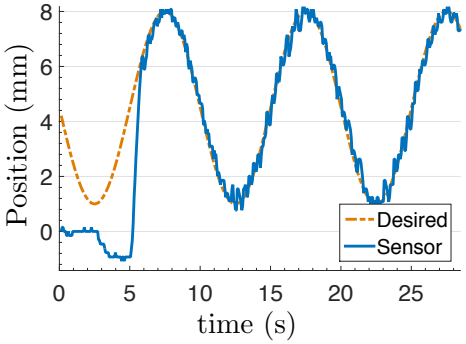

FIGURE 5.16: Sinusoid tracking using 14 coils/cm sensor.

5.3.1 Data on Additional Applications

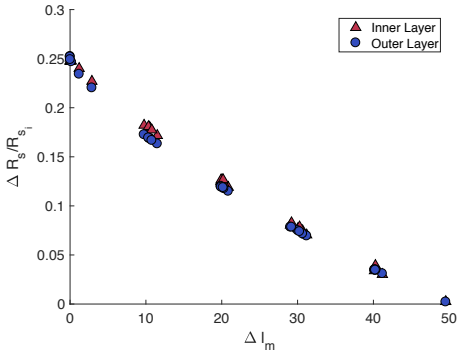

FIGURE 5.17: Resistance vs Length of Stretch Band. The graph shows the 14.17 coils/cm multilayer sensor in Figure 5.7(i), expanded axially using the setup in figure 4.10.

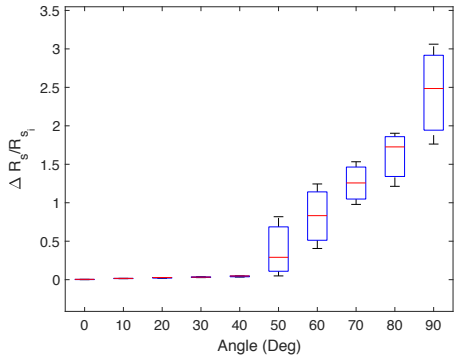

FIGURE 5.18: Resistance vs Finger Angle. The plot shows an experiment of a sensor covering the first and second knucles. The angle used is the second knuckle counting from the tip of the finger. The graph shows the 14 coils/cm multilayer sensor in Figure 5.7(i), expanded axially using the setup in figure 4.10.

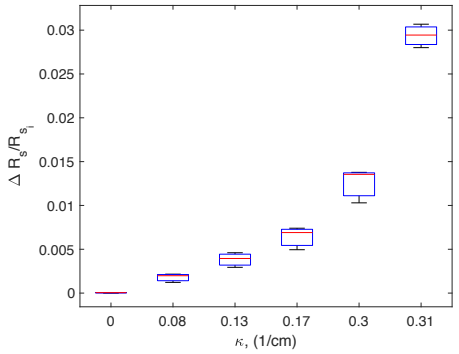

FIGURE 5.19: Resistance vs Radius of Curvature. The graph shows the 14 coils/cm multilayer sensor in Figure 5.7(i), expanded axially using the setup in figure 4.10.

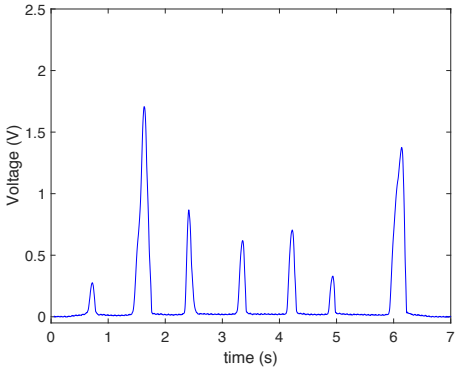

(a) Loadcell Force Output in Voltage.

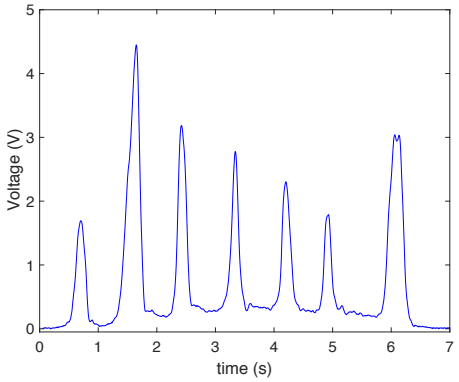

(b) Finger Sensor Output in Voltage.

FIGURE 5.20: Sensor Voltage vs time. (a) Load cell voltage vs time. (b) Sensor voltage vs time.

Chapter 6

CONCLUSIONS

6.1 DISCUSSION

In this thesis, I have presented a systematic manufacturing process of a 3D soft sensor. The manufacturing process involved a method to create thin cylindrical polymer structures, 3D structure eGaIn writing, and full pattern encapsulation. The ability to build a 3D-structure soft sensor with a single system and without molds was demonstrated. The manufacturing process shows versatility in size of sensors and coil density. The 3 modes of cylindrical coordinates were characterized for the sensor. For a 4 mm axial displacement of the mechanism, a diametrical displacement of 10 mm is obtained. A maximum change in resistance of 20 Ω over 10 mm change is produced. This demonstrates an approximate sensitivity of 2 Ω/mm which is four times as sensitive than in previous work [17]. When testing for axial expansion, the maximum change was of about 0.2 Ω for a range of 10 mm change with a small hysteresis loop of 0.05 Ω maximum difference. In addition, torsion was also characterized, with a minimal change of 0.05 Ω for a range of 180 degrees in the specified setup. This means that this sensor effectively measures diametric change, whereas axial and torsional change are measurable possibly with amplification. Figs. 5.11, 5.12, and 5.13 show the comparison of measured data with models of how the muscle geometry and sensor resistance change. High coeffecients of determination, R^2, indicate that the models are accurate and that the sensor provides a force-independent measurement of muscle length.

In addition, controllability of a sensor-package has been shown. Although asymptotic stability is shown in the analysis with (4.21), (4.22), the controller reaches an ultimate bound due to the limitations of our system. The computational limitation of arduino is the main factor that limits the frequency of our actuators. The other limitation is the resolution, which is restricted to 10-bit. Other than our limitations, sliding mode

performs well in our system due to the inherent high frequency of the air valves used to inflate and deflate the muscle. The dynamics of the muscle are such that damping is also inherent in the system, so minimal overshoot and settling time are seen. The discrepancy of our sensor with the ground truth measurement was measured repeatedly. The discrepancy persists with negligible difference, meaning that calibration needs to be improved, but the sensor outputs repeatable values even under the influence of high frequency variations of air pressure.

Applications of the sensor were also presented.The strechband test demonstrates the ability of a multilayered sensor, and hence a single layered one, to accurately measure radial change for large axial deformations. The finger test shows that the sensor could be used for body tracking applications. The backbone test shows the ability of the sensor to work for bending applications. This sensor could be used to track the position of the backbone of a soft robot. Finally, the loadcell test shows that the sensor cannot only be used for position tracking but for pressure sensing as well.

6.2 FUTURE WORK

In the future, a more robust method of interfacing with electrical connectors will be implemented. Higher coil density will be pursued. Versatility of pattern writing during the manufacturing process will be shown. More extensive characterization of statics and dynamics of the Sensor-PAM system will be derived. A microcontroller with higher resolution and more computational power and possibly filtering will be used to improve performance. A force control method will be developed. The muscle-sensor package will be integrated to a robotic system for manipulation. The applications presented in this thesis will be pursued more in depth.

Bibliography

[1] Georgios Andrikopoulos, Georgios Nikolakopoulos, and Stamatis Manesis. A survey on applications of pneumatic artificial muscles. In *Control & Automation (MED), 2011 19th Mediterranean Conference on*, pages 1439–1446. IEEE, 2011.

[2] Frank Daerden and Dirk Lefeber. Pneumatic artificial muscles: actuators for robotics and automation. *European journal of mechanical and environmental engineering*, 47(1):11–21, 2002.

[3] Ching-Ping Chou and Blake Hannaford. Measurement and modeling of mckibben pneumatic artificial muscles. *IEEE Transactions on robotics and automation*, 12 (1):90–102, 1996.

[4] Michael Wehner, Brendan Quinlivan, Patrick M Aubin, Ernesto Martinez-Villalpando, Michael Baumann, Leia Stirling, Kenneth Holt, Robert Wood, and Conor Walsh. A lightweight soft exosuit for gait assistance. In *Robotics and Automation (ICRA), 2013 IEEE International Conference on*, pages 3362–3369. IEEE, 2013.

[5] Yong-Lae Park, Bor-rong Chen, Néstor O Pérez-Arancibia, Diana Young, Leia Stirling, Robert J Wood, Eugene C Goldfield, and Radhika Nagpal. Design and control of a bio-inspired soft wearable robotic device for ankle–foot rehabilitation. *Bioinspiration & Biomimetics*, 9(1):016007, 2014.

[6] A Hildebrandt, O Sawodny, R Neumann, and A Hartmann. Cascaded control concept of a robot with two degrees of freedom driven by four artificial pneumatic muscle actuators. In *Proceedings of the 2005, American Control Conference, 2005.*, pages 680–685. IEEE, 2005.

[7] Hugh M Herr and Roy D Kornbluh. New horizons for orthotic and prosthetic technology: artificial muscle for ambulation. In *Smart structures and materials*, pages 1–9. International Society for Optics and Photonics, 2004.

[8] DG Caldwell, GA Medrano-Cerda, and MJ Goodwin. Braided pneumatic actuator control of a multi-jointed manipulator. In *Systems, Man and Cybernetics,*

1993.'Systems Engineering in the Service of Humans', Conference Proceedings., International Conference on, pages 423–428. IEEE, 1993.

[9] Yong-Lae Park, Bor-rong Chen, Diana Young, Leia Stirling, Robert J Wood, Eugene Goldfield, and Radhika Nagpal. Bio-inspired active soft orthotic device for ankle foot pathologies. In *2011 IEEE/RSJ International Conference on Intelligent Robots and Systems*, pages 4488–4495. IEEE, 2011.

[10] Yiğit Mengüç, Yong-Lae Park, Ernesto Martinez-Villalpando, Patrick Aubin, Miriam Zisook, Leia Stirling, Robert J Wood, and Conor J Walsh. Soft wearable motion sensing suit for lower limb biomechanics measurements. In *Robotics and Automation (ICRA), 2013 IEEE International Conference on*, pages 5309–5316. IEEE, 2013.

[11] Daniel Vogt, Yong-Lae Park, and Robert J Wood. A soft multi-axis force sensor. In *Sensors, 2012 IEEE*, pages 1–4. IEEE, 2012.

[12] Yong-Lae Park, Carmel Majidi, Rebecca Kramer, Phillipe Bérard, and Robert J Wood. Hyperelastic pressure sensing with a liquid-embedded elastomer. *Journal of Micromechanics and Microengineering*, 20(12):125029, 2010.

[13] Yong-Lae Park, Bor-rong Chen, and Robert J Wood. Soft artificial skin with multi-modal sensing capability using embedded liquid conductors. In *Sensors, 2011 IEEE*, pages 81–84. IEEE, 2011.

[14] Yong-Lae Park, Bor-Rong Chen, and Robert J Wood. Design and fabrication of soft artificial skin using embedded microchannels and liquid conductors. *IEEE Sensors Journal*, 12(8):2711–2718, 2012.

[15] J William Boley, Edward L White, George T-C Chiu, and Rebecca K Kramer. Direct writing of gallium-indium alloy for stretchable electronics. *Advanced Functional Materials*, 24(23):3501–3507, 2014.

[16] Joseph T Muth, Daniel M Vogt, Ryan L Truby, Yiğit Mengüç, David B Kolesky, Robert J Wood, and Jennifer A Lewis. Embedded 3d printing of strain sensors within highly stretchable elastomers. *Advanced Materials*, 26(36):6307–6312, 2014.

[17] Yong-Lae Park and Robert J Wood. Smart pneumatic artificial muscle actuator with embedded microfluidic sensing. In *SENSORS, 2013 IEEE*, pages 1–4. IEEE, 2013.

[18] Michael D. Dickey, Ryan C. Chiechi, Ryan J. Larsen, Emily A. Weiss, David A. Weitz, and George M. Whitesides. Eutectic gallium-indium (EGaIn): A liquid metal alloy for the formation of stable structures in microchannels at room temperature.

Advanced Functional Materials, 18(7):1097–1104, 2008. ISSN 1616-3028. doi: 10.1002/adfm.200701216. URL http://dx.doi.org/10.1002/adfm.200701216.

[19] R Adam Bilodeau, Edward L White, and Rebecca K Kramer. Monolithic fabrication of sensors and actuators in a soft robotic gripper. In *Intelligent Robots and Systems (IROS), 2015 IEEE/RSJ International Conference on*, pages 2324–2329. IEEE, 2015.

[20] W. Felt, K. Y. Chin, and C. D. Remy. Contraction sensing with smart braid mckibben muscles. *IEEE/ASME Transactions on Mechatronics*, 21(3):1201–1209, June 2016. ISSN 1083-4435. doi: 10.1109/TMECH.2015.2493782.

[21] O. Erin, N. Pol, L. Valle, and Y.-L. Park. Design of a bio-inspired pneumatic artificial muscle with self-contained sensing. *International Conference of the IEEE Engineering in Medicine and Biology Society (EMBC'16)*, 21(3):1201–1209, June 2016. ISSN 1083-4435. doi: 10.1109/TMECH.2015.2493782.

[22] HK Moffatt. Behaviour of a viscous film on the outer surface of a rotating cylinder. 1977.

[23] Qin Xu, Nikolai Oudalov, Qiti Guo, Heinrich M Jaeger, and Eric Brown. Effect of oxidation on the mechanical properties of liquid gallium and eutectic gallium-indium. *Physics of Fluids*, 24(6):063101, 2012.

[24] Raymond Mulley. *Flow of industrial fluids: theory and equations*. CRC Press, 2004.

[25] Yuri Shtessel, Christopher Edwards, Leonid Fridman, and Arie Levant. *Sliding mode control and observation*. Springer, 2014.